PROCEEDINGS OF SPIE

SPIEDigitalLibrary.org/conference-proceedings-of-spie

# The High-contrast End-to-End Performance Simulator (HEEPS): influence of ELT/METIS instrumental effects

Christian Delacroix, Olivier Absil, Gilles Orban de Xivry, Muskan Shinde, Prashant Pathak, et al.

Christian Delacroix, Olivier Absil, Gilles Orban de Xivry, Muskan Shinde, Prashant Pathak, Faustine Cantalloube, Brunella Carlomagno, Valentin Christiaens, André Boné, Dennis Dolkens, Matthew Kenworthy, David Doelman, "The High-contrast End-to-End Performance Simulator (HEEPS): influence of ELT/METIS instrumental effects," Proc. SPIE 12187, Modeling, Systems Engineering, and Project Management for Astronomy X, 121870F (25 August 2022); doi: 10.1117/12.2630341

SPIE.

Event: SPIE Astronomical Telescopes + Instrumentation, 2022, Montréal, Québec, Canada

# The High-contrast End-to-End Performance Simulator (HEEPS): influence of ELT/METIS instrumental effects

Christian Delacroix*[a], Olivier Absil[a], Gilles Orban de Xivry[a], Muskan Shinde[b], Prashant Pathak[a], Faustine Cantalloube[c], Brunella Carlomagno[a], Valentin Christiaens[a], André Boné[d], Dennis Dolkens[e], Matthew Kenworthy[f], David Doelman[f]

[a] Space sciences, Technologies, and Astrophysics Research (STAR) Institute, Université de Liège, Allée du Six Août 19C, 4000 Liège, Belgium
[b] Indian Institute of Science Education and Research (IISER) Pune, Dr. Homi Bhabha Rd, Pashan, Pune 411008, India
[c] Laboratoire d'Astrophysique de Marseille, 38 Rue Frédéric Joliot Curie, 13013 Marseille, France
[d] Max-Planck-Institut für Astronomie (MPIA), Königstuhl 17, 69117 Heidelberg, Germany
[e] NOVA Optical Infrared Astronomical Instrumentation Group, Oude Hoogeveensedijk 4, 7991 PD Dwingeloo, The Netherlands
[f] Leiden Observatory, Leiden University, PO Box 9513, 2300 RA Leiden, The Netherlands

## ABSTRACT

The High-contrast End-to-End Performance Simulator (HEEPS) is an open-source python-based software with a modular and extensible architecture, that creates end-to-end simulations of high contrast imaging (HCI) instruments. It uses the wavefront Fresnel propagation package PROPER, the telescope instrument data simulator ScopeSim, and the HCI image processing package VIP. In this paper, we present the design of HEEPS, and motivate its baseline structure with the implementation of the Mid-infrared ELT Imager and Spectrograph (METIS) HCI modes, including coronagraphic components such as vortex phase masks, ring apodizers, and apodizing phase plates. Then, we present the key results of our thorough end-to-end simulations starting from 1-hour AO residual phase screens produced with the end-to-end AO simulator COMPASS. We analyze various undesirable effects such as pupil effects (stability, uniformity, drift) and non-common path phase and amplitude errors. Finally, the coronagraphic performance including all effects is shown for all the METIS HCI modes as 5-sigma sensitivity contrast curves after ADI post-processing.

**Keywords:** end-to-end simulation, extremely large telescope, mid-infrared instrumentation, high-contrast imaging, vortex coronagraph, ELT/METIS

## 1. INTRODUCTION

The Mid-infrared ELT Imager and Spectrograph (METIS)[1] will provide high-contrast imaging at L (2.9-4.1 μm), M (3.9-5.3 μm), and N (8.0-13.5 μm) bands, using advanced coronagraphic techniques like vortex coronagraphs[2,3] and apodizing phase plates[4]. In terms of contrast performance requirement, the METIS coronagraphs shall deliver a 5σ contrast at L-band of $3\times10^{-5}$ at a distance of $5\lambda/D$ from a bright star ($L \leq 6$ mag) within one hour of on-target integration time, under median seeing conditions and after post-processing. Because it pertains to post-processed contrast, this requirement can only be verified by simulating the full observing and data analysis chain. To this end, we have developed an end-to-end performance simulator, referred to as High-contrast ELT End-to-end Performance Simulator (HEEPS)[5].

*cdelacroix@uliege.be; star.uliege.be

Modeling, Systems Engineering, and Project Management for Astronomy X, edited by George Z. Angeli, Philippe Dierickx, Proc. of SPIE Vol. 12187, 121870F
 · 0277-786X · doi: 10.1117/12.2630341

In Section 2, we provide an overview of the HEEPS simulation pipeline. In Section 3, we describe the nominal HCI performance in presence of AO residuals. We present the influence of various undesirable instrumental effects in Section 4, and the combination of all effects is shown in Section 5. Finally, we summarize our conclusions in Section 6.

## 2. HEEPS SIMULATION PIPELINE

The HEEPS simulation pipeline involves the following steps depicted in Figure 1: (i) obtain a temporal series of single-conjugate adaptive optics (SCAO) residual phase screens from an end-to-end AO simulation tool (COMPASS)[6], (ii) propagate the SCAO residual phase screens through the METIS HCI elements using an optical propagation tool (PROPER)[7], taking into account other environmental or instrumental effects, (iii) use the obtained instantaneous coronagraphic PSFs to produce a mock Angular Differential Imaging (ADI)[8] observing sequence (pupil tracking mode observations), taking into account the METIS radiometric budget from ScopeSim and the field rotation for a representative HCI target, and (iv) use the Vortex Image Processing (VIP)[9] package to compute the performance in terms of post-processed contrast (see definition below).

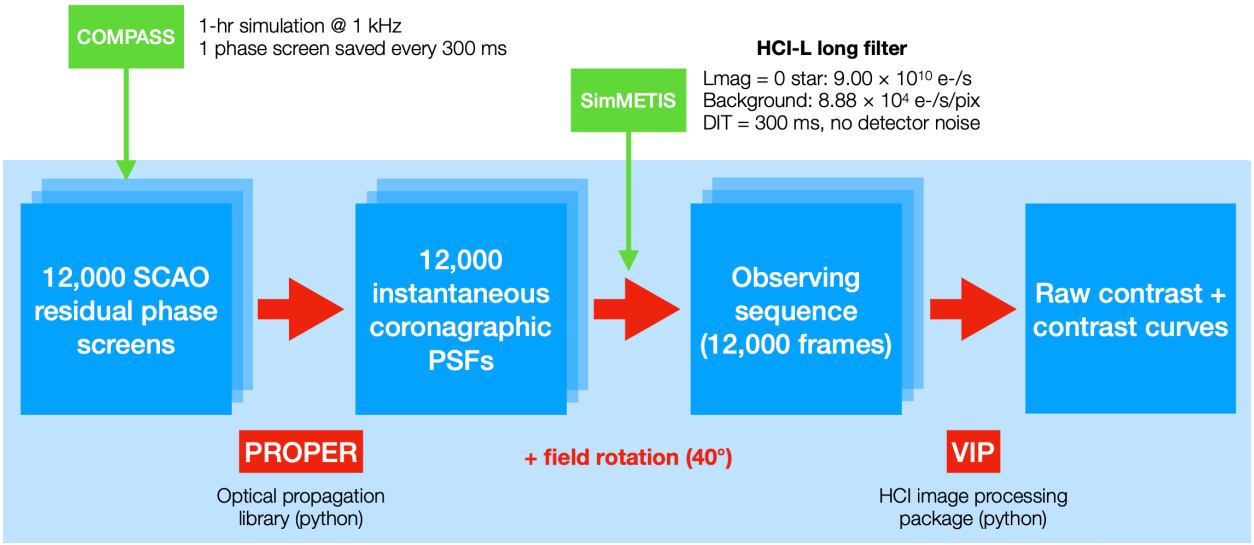


Figure 1: HEEPS simulation pipeline.

A standard HEEPS simulation assumes a latitude of -24.59° (at Cerro Armazones) and a declination of -5°, which provides a parallactic angle rotation of about 40° in a 1-h ADI sequence. For this 1-h baseline, the best sampling that we can use while maintaining a reasonable CPU time and a reasonable RAM usage is about 100 msec, which gives a total of 36,000 phase screens. The computation time is then of a few days for the SCAO simulation on a standard GPU server, about 1-3 h for the optical propagation on a 56-core CPU server, and about 3-5 h for the contrast curve computation. The RAM usage for the optical propagation and contrast curve computation can be kept below the 252 Gb available on our CPU server.

As shown by Carlomagno et al.[5], the degradation in performance associated with a down-sampling from 100 to 300 msec is still generally not larger than a factor 2, which we deem acceptable. In order to reduce the required computation time for the following study, we use a 1-h long sequence with 300 msec sampling (12,000 phase screens). SCAO-limited performance will therefore be slightly pessimistic in the following results (by a factor ~2).

# 3. NOMINAL HCI PERFORMANCE IN PRESENCE OF AO RESIDUALS

In this section, we describe the "nominal" HCI performance of METIS in presence of thermal background noise for typical stellar magnitudes, taking into account SCAO residual phase screens as the only perturbation to the system, assuming the instrument to be otherwise perfect. The sensitivity limits produced here will be used as a reference for the exploration of instrumental and environmental parameters in the next sections.

## 3.1 Definition of contrast

Before discussing the HCI performance of METIS, it is important to define the metrics used to evaluate the performance. The main metric used in this paper is the post-processed **5σ sensitivity (contrast)**, as defined in Mawet et al. 2014[10]. This definition is based on the analysis of the final image obtained after post-processing of an ADI observing sequence. Here, we will generally stick to a classical ADI post-processing algorithm (temporal median subtraction, image derotation, and mean combination). The noise level in the final image is computed at a given angular separation from the star as the standard deviation of the aperture fluxes measured in as many independent resolution elements as can be defined at that separation. In order to evaluate the sensitivity limit of the instrument in terms of contrast, this noise level must then be compared to the non-coronagraphic signal of the host star, taking into account the throughput of the post-processing algorithm. This throughput is evaluated by injecting fake companions at various positions into the raw data and by applying the same post-processing algorithm to measure the amount of signal preserved in the final post-processed image. The formula defining the 5σ contrast is the following:

$$c = \frac{5\sigma}{\tau S} \ , \tag{1}$$

where σ is the noise standard deviation, S the non-coronagraphic stellar signal measured in an aperture of size equal to one resolution element (λ/D), and τ the algorithm throughput. Note that the factor 5 is associated to a fixed false alarm probability ($3\times10^{-7}$) for purely Gaussian noise. Beyond the fact that noise might not be purely Gaussian after ADI post-processing, the small number of samples at short angular separations modifies the relation between false alarm probability and noise level. In order to keep the same false alarm probability at all separations, this requires to modify the definition of contrast, taking into account a t-Student distribution[10] instead of a standard Gaussian distribution. The penalty associated to small sample statistics is taken into account in all contrast curves presented in this paper.

While the 5σ contrast is used to verify the METIS requirement, we will also show the raw contrast for some results in this paper, to help illustrate specific effects. The **raw contrast** is defined, at any given separation, as the ratio between the intensity of the considered PSF (be it coronagraphic or not) and the peak of the non-coronagraphic PSF. It indicates the mean level of residual starlight at a given separation. Raw contrast can readily be assessed by plotting the PSF profile of interest in a figure where the direct PSF profile culminates at 1 on the optical axis. This metric does not tell what is the faintest source that can be detected, as it is not a direct indicator of noise level. Yet, raw contrast is useful to assess a coronagraph's capability to cancel stellar light.

## 3.2 L-band performance

Using a 1-h SCAO sequence with 300-msec sampling, we perform a first set of simulations at L band (central wavelength of 3.8 μm) for the three coronagraphic concepts included in the METIS baseline: the Classical Vortex Coronagraph (CVC), the Ring Apodized Vortex Coronagraph (RAVC), and the Apodizing Phase plate (APP). In Figure 2, we show representative instantaneous PSFs for the three coronagraphic concepts, as well as the long-term PSF, averaged over the full 1-h sequence. This figure clearly highlights the well-corrected region corresponding to the spatial frequencies that can be controlled by the ELT deformable mirror (about $76\lambda/D$ across). It also highlights the amount of starlight remaining in the science focal plane, ranging from full stellar light in the case of the APP, to very low starlight for the RAVC. The mean total stellar leakage for the CVC and RAVC in presence of AO residuals is respectively around 4.7% and 2.4%. These figures are due to the combination of diffraction in the telescope with atmospheric turbulence. In the absence of any perturbation, the total stellar leakage for these two configurations, due exclusively to diffraction effects associated with the shape of the input pupil (and to the Lyot stop design), would amount to 2.6% (CVC) and 0.2% (RAVC). The level of

residual starlight should also be compared with other fundamental contributors to the total stellar leakage, such as the chromaticity of the Vortex Phase Mask (VPM) (total leakage below 0.2% at L band), the influence of atmospheric dispersion (total leakage below 1% on HCI-compliant filters), or the influence of partially resolved stellar surfaces (total leakage of 4% for α Cen A, one of the worst cases for METIS HCI). The results presented here are valid for sufficiently low air masses, or equivalently for sufficiently narrow filters (bandwidth < 10%), and for sufficiently small stars (angular diameter smaller than 4 mas at L band), in which cases the effect of atmospheric dispersion and of partly resolved stellar surfaces is reduced below the level of stellar leakage associated to pure atmospheric turbulence.

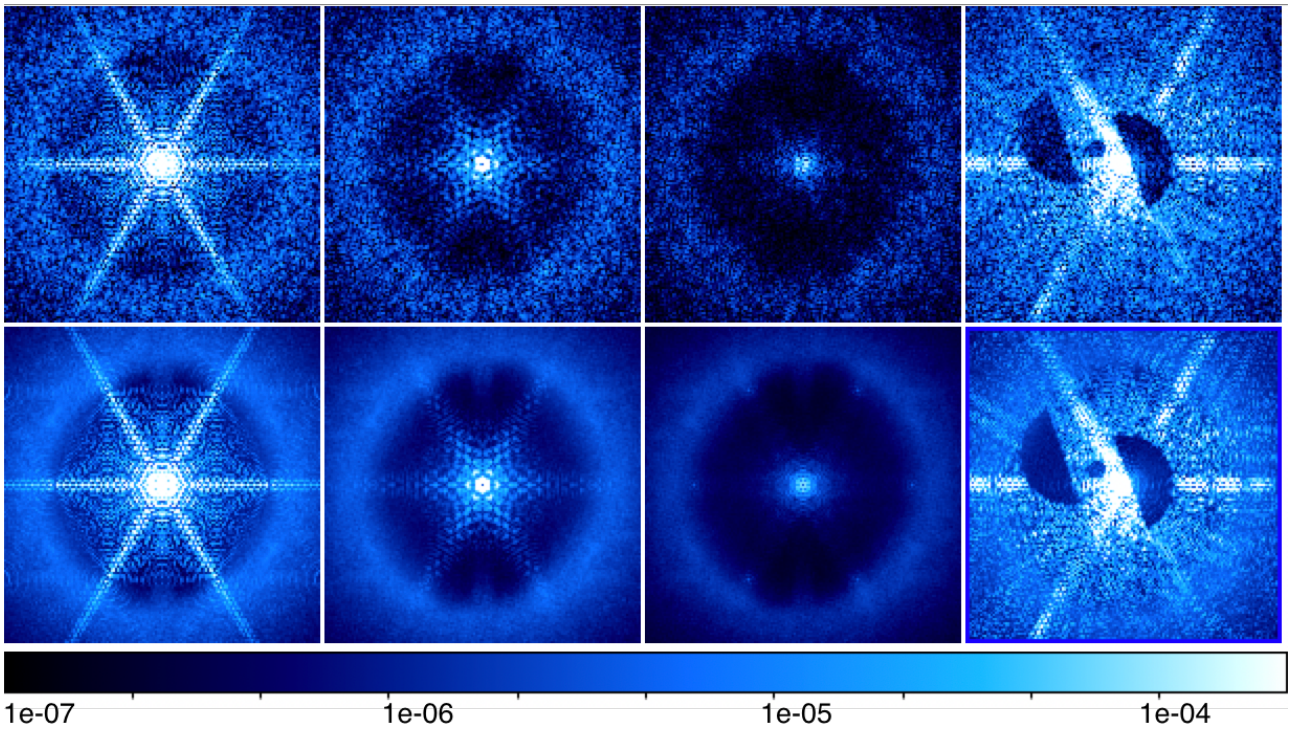


Figure 2: *Top.* Representative instantaneous PSFs at L band, using a single SCAO residual phase screen, obtained in the case of direct imaging (left), CVC (middle-left), RAVC (middle-right), and APP (right). *Bottom.* Same for long-exposure PSFs. All images have been cropped to a field-of-view of $100\lambda/D$, i.e., 2.″1 at L band.

The raw PSF profiles (a.k.a. *raw contrast*) and the 5σ sensitivity limits in terms of flux ratio after ADI post-processing (a.k.a. *contrast curves*) are displayed in Figure 3. It illustrates well the specific features of each mode, with the RAVC providing the deepest starlight cancellation. Note that all optical propagations performed in this paper use the actual ELT-M1 exit pupil shape, including spider arms and segments.

In the case of the APP, the raw and post-processed contrasts were computed by combining the dark holes associated with the two coronagraphic PSFs of the grating-vector APP. This leaves in principle a bright stripe of speckles in between the two dark holes. Here, we have artificially dimmed this bright stripe to facilitate the contrast computation. The contrast curves for the APP are thus somewhat optimistic, especially at the shortest separations where the bright stripe has the largest relative influence. A more advanced way to compute contrast curves for the APP will be implemented during METIS Phase D, in parallel with the pipeline development.

While a Classical Lyot Coronagraph (CLC) is included in this figure for the sake of completeness, this back-up observing mode will not be systematically investigated in the present paper, because its performance does not need to meet any specific requirement (it is not a baseline observing mode for METIS).

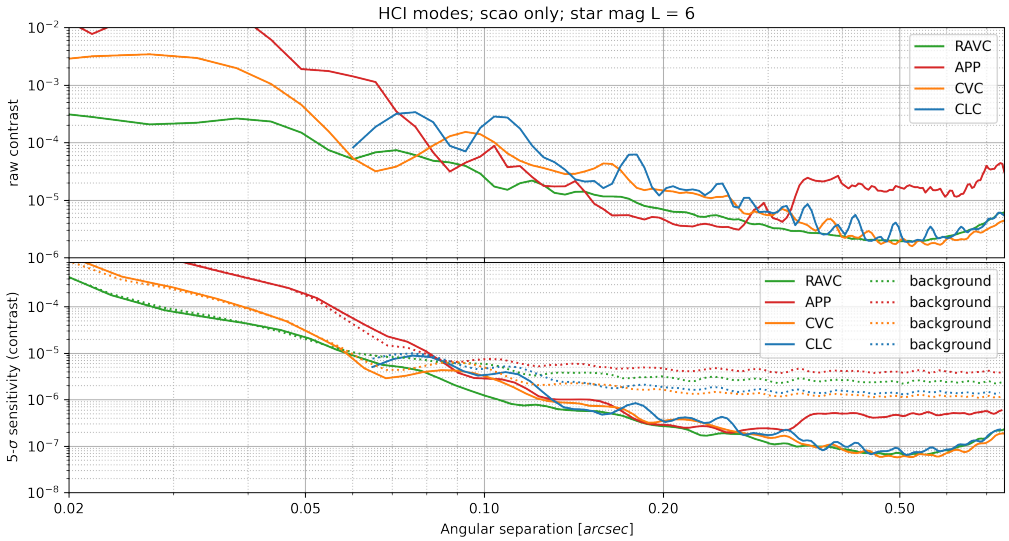


Figure 3: Raw contrast (top) and ADI contrast curve (bottom) for the RAVC, CVC, APP, and CLC observing modes at L band. In the bottom plot, the solid curves include only the contribution of speckle noise, while the dashed curves include the effect of the thermal background (shot noise) for a star of magnitude $L = 6$.

All HCI modes meet the contrast requirement in this simple simulation including only residual SCAO phase screens. This situation is expected to change in presence of instrumental errors: while random atmospheric speckles efficiently average out over the 1-h observing sequence, instrumental errors are expected to create long-lived speckles whose intensity is modulated by the stellar diffraction pattern. It is noteworthy that the sensitivity limits become dominated by thermal background noise beyond about 0.″15 (or even closer for the RAVC), for the stellar magnitude $L = 6$ considered here. Further simulations show that, for $L = 8$, the transition between the speckle-dominated and the background-dominated regimes shifts to about 0.″1 (i.e., $5\lambda/D$). Using a coronagraph for fainter targets becomes less and less useful. The CVC provides the best sensitivity limits in the background-limited regime, thanks to its superior throughput. The throughput of the various modes takes into account the pure transmission of the associated pupil stops, the transmission of optical elements (vortex phase mask, APP), the Strehl ratio of the (off-axis) PSF, as well as the division of the flux into two parts for the APP (or more precisely three parts, as the leakage terms receives a few percent of the total flux). This leads to a total throughput of about 14% for the APP, 16% for the RAVC, 48% for the CLC, and 53% for the CVC, relative to the throughput of a hypothetical imaging mode that would not feature any cold pupil stop. In practice, the default imaging mode of METIS in pupil tracking has a half-maximum encircled energy throughput of about 67%.

### 3.3 M-band performance

The same analysis as in L band is carried out at M band in Figure 4. The improvement in contrast due to the phase errors scaling with wavelength is largely compensated by the loss in angular resolution, leading to similar performance as a function of separation expressed in arcsec. In presence of thermal background and photon noise, the performance is largely decreased compared to L band, due to the higher background level at M band. This also means that the RAVC becomes less useful at this wavelength, and will only be used for stars significantly brighter than $M = 6$.

### 3.4 N-band performance

Because of the large thermal background, coronagraphy at N band will only be useful for the brightest target stars. Here, we therefore focus on the case of α Cen A, with magnitude $N = -1.6$. For the sake of simplicity, we keep the same set of SCAO residual phase screens, as well as the same trajectory in the sky, although we recognize that a 1-h observing sequence on α Cen would actually lead to a parallactic angle variation of only about 23° (instead of 40°).

The sensitivity limits at 11.5 µm (a.k.a. N2 band) are displayed for α Cen A in Figure 5. They show that, even for one of the brightest stars in the sky, the performance is background limited for angular separations larger than about 0.″5. Because the RAVC largely decreases the total throughput, this mode is not considered at N band. Indeed, additional simulations show that, even for a bright star like α Cen, the RAVC would improve HCI performance only within about 0.″1. A simple CVC is preferred at N band to provide the highest possible throughput, while still reducing the total amount of stellar light from the host star by a factor ∼30, and the peak intensity in any pixel by a factor slightly larger than 100.

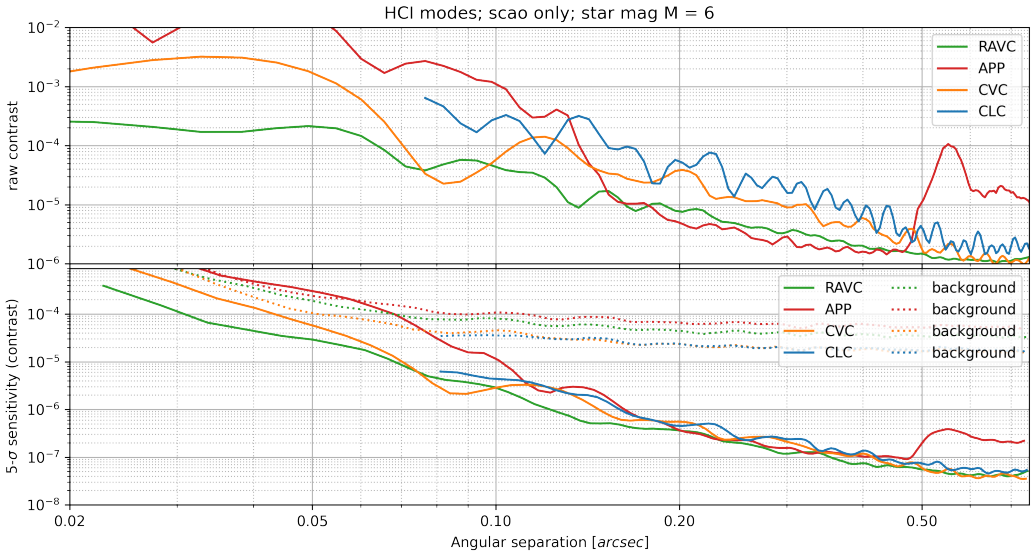


Figure 4: Same as Figure 3 for M band, in the case of a star of magnitude $M = 6$.

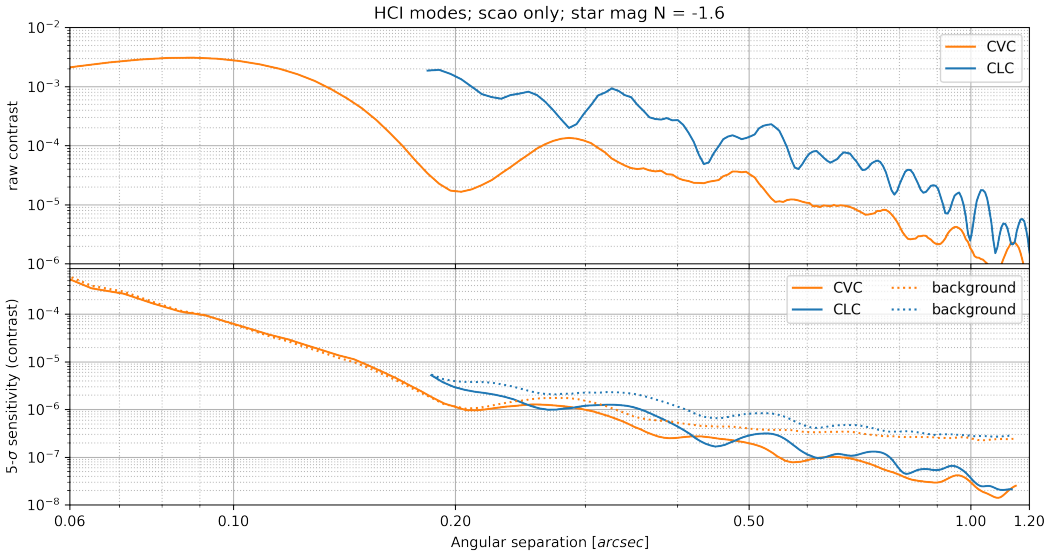


Figure 5: Same as Figure 3 for N2 band (around 11.5 µm), in the case of a star of magnitude $N = -1.6$.

# 4. INFLUENCE OF VARIOUS INSTRUMENTAL EFFECTS

In this section, we investigate the influence of various instrumental effects, which directly affect HCI performance. This is the only practical way to define requirements on various noise sources in order to meet the contrast requirement. Yet, we caution the reader about the limitations of this study. First, simulations are inherently limited by the physical phenomena taken into account. We need to acknowledge the fact that known unknowns and unknown unknowns may affect the final performance that METIS will actually deliver on sky. In order to define requirements on individual noise sources and disturbances, our simulation strategy is to first explore each noise source individually, and to use a general rule of thumb that any individual contributor should produce a post-processed contrast 10 times below the $3\times10^{-5}$ top-level requirement, i.e., a post-processed contrast of $3\times10^{-6}$ at a distance of $5\lambda/D$. For each noise source, we explore various perturbation levels and/or compare our best estimate of the performance degradation to this internal requirement. In a second step, all effects are combined in a global simulation to explore the overall performance of the METIS HCI modes (taking into account possible cross-talk between the various effects), and to check whether it complies with our top-level requirement.

## 4.1 Influence of pupil shape (misaligned segments)

The ELT-M1 primary mirror is not coronagraphy-friendly, due to the presence of a big central obscuration, secondary support structures, and segments. All these features have a large impact on HCI performance, all the more that the image of the ELT pupil is not stabilized in position and rotation in the first accessible pupil plane within METIS, where the effects of diffraction could have been handled by advanced apodizer designs (pupil derotation and stabilization are implemented downstream of the first pupil plane for practical reasons). Both APP and RAVC have been optimized to mitigate the effect of the 30% central obscuration, but the spiders and the complex ELT-M1 pupil shape still represent important sources of spurious diffracted light. This is particularly true for the vortex coronagraph, because the Ring Apodizer (RAP) is located ahead of the derotator, so that it cannot be optimized to handle starlight diffracted by spider arms or pupil edge. Conversely, the APP is optimized to take into account the effect of the complex pupil shape (including spiders), because it is positioned after the derotator, in a pupil plane where the image of the ELT pupil is stabilized. The spiders have two effects: on one hand, they lead to additional diffracted stellar light inside the Lyot stop, and on the other hand, their associated thermal emission increases the background emission if not properly masked by the cold Lyot stop. Thanks to the stabilization of the ELT pupil inside METIS, the image of the spiders can be masked at the Lyot stop / APP level with a reasonable level of oversizing: for 54-cm spiders in the ELT pupil plane (1.4% of the nominal pupil diameter), the spider width in the Lyot stop / APP plane amounts to about 4% of the nominal pupil diameter (i.e., about 150 cm in the ELT-M1 pupil), taking into account the effects of pupil alignment, stability, and blurring.

Besides spiders and pupil edges, mirror segmentation can also lead to performance degradation. Segmentation itself creates spurious replica of the ELT PSF within the coronagraphic images. These aliases however appear at spatial frequencies higher than the frequencies that can be corrected by the M4 deformable mirror. They will therefore be located in a region where HCI performance is severely reduced, and are thus not considered as a critical issue here. The real problem with mirror segmentation is that, during night-time operations, several mirror segments could be misaligned due to maintenance. The average number of misaligned segments will be no more than seven during the ELT lifetime. The most probable spatial distribution of misaligned segments is a flower pattern (i.e., seven neighbouring segments, see Figure 6 left) due to a failure within a segment concentrator. Because these misaligned segments may change from night to night, it is impossible to optimize the coronagraphs to compensate for them. Assuming that the misaligned segments will be pointed towards an empty sky region, far enough from the bright target star, their net effect is to create a “hole” in the starlight intensity distribution in the input pupil. This hole will create additional diffracted starlight inside the Lyot stop, leading to additional stellar leakage in the coronagraphic PSF (see Figure 6).

Figure 7 shows the contrast curves in presence of one or two sets of seven misaligned segments, arranged in a flower pattern. In this configuration, the effect of misaligned segments starts to show at angular separations larger than about 0.″06. At $5\lambda/D$ (i.e., 0.″1), where the contrast requirement is defined, the ADI contrasts is degraded by a factor around 3, in the case where one set of misaligned segments is located in the outer part of the pupil defined by the Lyot stop of the RAVC. While the ADI contrast performance is still marginally compliant with our goal ($3\times10^{-6}$), it would clearly be preferable to operate the METIS HCI modes in the absence of misaligned segments. We note that the presence of

misaligned segments in the inner part of the pupil (blocked by the RAVC Lyot stop) does not significantly impact the RAVC performance.

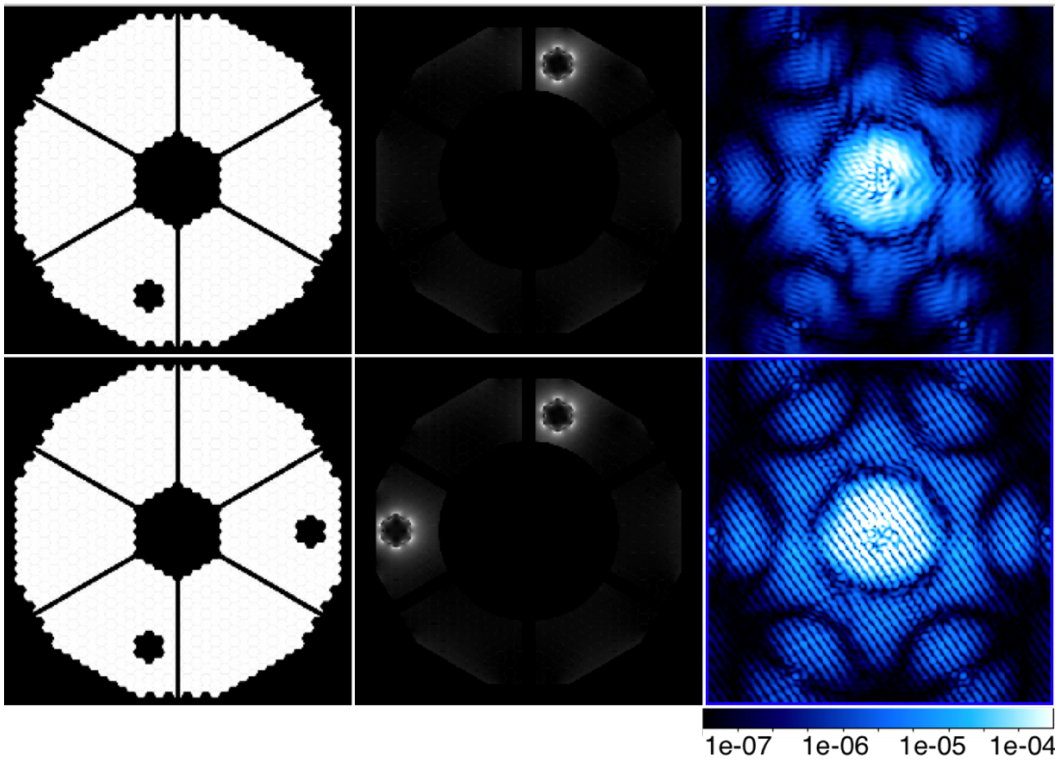


Figure 6: *Left*. Input pupil with seven misaligned segments in flower configuration. *Middle.* Corresponding distribution of light in the Lyot stop plane for the RAVC. *Right.* Averaged noiseless coronagraphic PSF, in presence of atmospheric turbulence.

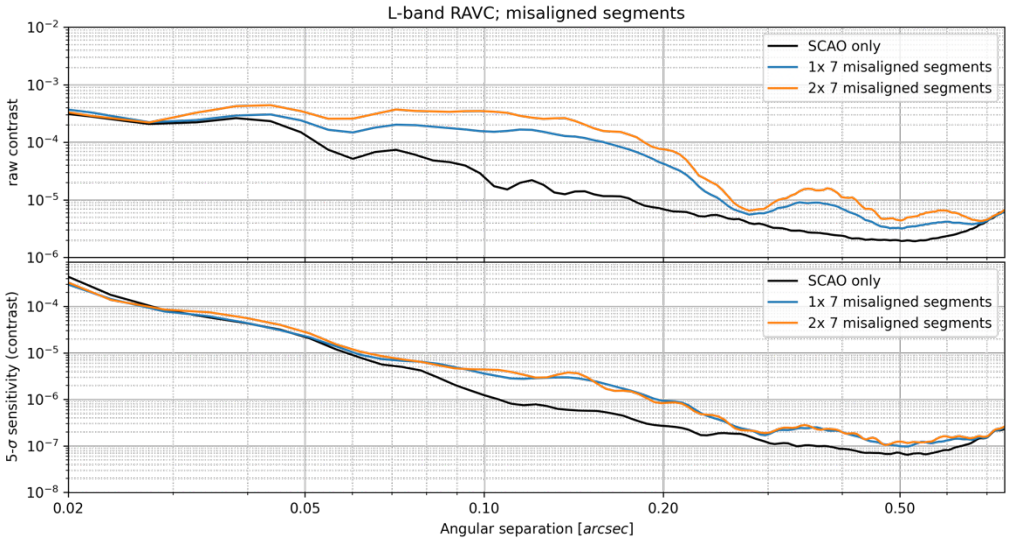


Figure 7: ADI contrast curves for the RAVC at L band in presence of residual atmospheric turbulence for various configurations of misaligned segments in the ELT pupil.

### 4.2 Influence of pupil uniformity (segment reflectivity)

In addition to the effect of its complex pupil shape, the ELT-M1 primary mirror is expected to produce a non-uniform pupil illumination, due to variations in the reflectivity of segments. The transmission non-uniformity across the pupil, not taking into account misaligned segments, is foreseen by ESO to be better than 10% Peak-to-Valley (PV). For a total of almost 800 segments, that PV level corresponds to a Gaussian distribution with standard deviation around 1.7%.

Figure 8 shows contrast curves in presence of various levels of non-uniform segment reflectivity, ranging from 1% to 3% rms, which is equivalent to about 5% to 15% PV. Because the spatial frequencies associated with pupil non-uniformity are quite high, the contrast curves are not affected. This effect is therefore not an issue for fulfilling the top-level HCI requirement.

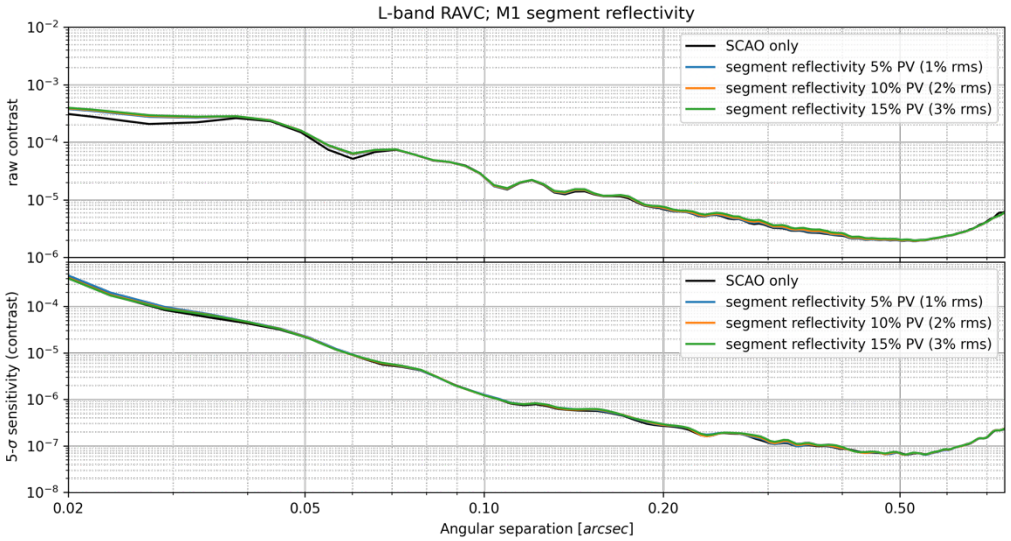


Figure 8: ADI contrast curves for the RAVC at L band in presence of various amounts of M1 segment non-uniformity in terms of reflectivity.

### 4.3 Influence of pupil stability (RAVC only)

Thanks to the pupil stabilization mechanism, the ELT pupil will be stabilized inside METIS with a relative accuracy of about 1%. This stabilization however occurs downstream of the pupil plane where the Ring Apodizer (RAP) is installed. This means that the RAP will be seen as drifting on top of the image of the ELT pupil, with an expected PV amplitude up to about 2.7% (requirement: 3%). Here, we investigate the effect of this drift on the METIS HCI performance. The residual drift of the ELT pupil image downstream of the pupil stabilization mirror will be compensated by oversizing/undersizing the Lyot stop appropriately, and will therefore not contribute significantly to the stellar leakage level (but will reduce the overall throughput). Based on the expected stability of the ELT pupil with respect to METIS, we have chosen to further oversize the central obscuration in the Lyot stop by about 3%, in addition to the 1% oversizing due to pupil image quality.

The effect of the misalignment of the RAP with respect to the input pupil and Lyot stop is illustrated in Figure 9. The additional amount of stellar leakage in the focal plane remains relatively low, as long as the footprint of the transition between the two zones in the RAP remains hidden behind the central obscuration of the Lyot stop. To simulate the effect of drifts in the ELT pupil position during an HCI observing sequence, drifts with PV amplitudes ranging from 1% to 5% of the M1 projected diameter were injected in the optical propagation of the phase screens. In our simulations, the RAP moves with respect to the ELT-M1 pupil image along the x axis, with a timescale equal to the duration of the ADI sequence. While the effect of this drift on the amount of stellar leakage is low (Figure 10, top), the effect on the ADI post-processed contrast is significant because of the deformations of the coronagraphic PSF associated to the changing intensity

distribution in the input pupil. By assuming that the drift happens on the same timescale as the ADI observing sequence, we are here investigating a worst-case scenario, as the variations in coronagraphic PSF shape will not be well captured by the median in the ADI processing, and will not average out sufficiently well on typically observing sequences. Under this hypothesis, a drift of 1% PV would already be very detrimental to the HCI performance at the shortest angular separations (see Figure 10, bottom). Yet, we can tolerate a drift of the ELT pupil of up to 3% PV with respect to the RAP inside METIS before reaching our self-defined requirement in terms of post-processed contrast in Figure 10. This is compatible with the expected stability of the ELT pupil at the level of the RAP pupil plane.

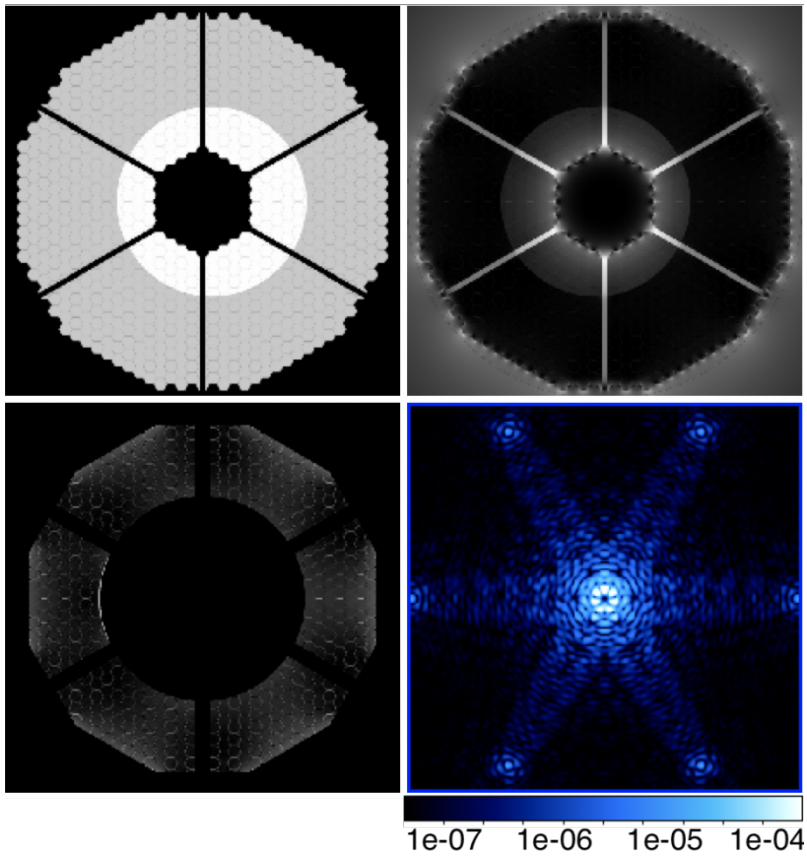


Figure 9: Effect of the ring apodizer misalignment on the RAVC behavior. The misalignment has been exaggerated to 5% here for the sake of illustration. *Top.* Illustration of the apodizer misalignment (left), and intensity distribution at the Lyot plane, just before the Lyot stop (right). *Bottom.* Intensity distribution at the Lyot plane, just after the Lyot stop (left), and associated coronagraphic PSF (right).

Any pupil drift happening at higher temporal frequencies, including pupil jitter due to vibration, will have a smaller influence on the HCI performance than the low-frequency drift simulated here, because they partly average out in ADI post-processing. The amplitude of pupil jitter is expected to be much smaller than 1% anyway, and will therefore not contribute significantly to the HCI performance budget. It must be noted that, whatever their amplitude, drifts of the ELT pupil with respect to METIS are an effect on which we have almost no control, and which we will need to live with. This effect will however **only affect the RAVC observing mode**, as long as ELT pupil drifts do not lead to any pupil vignetting at the first pupil plane, where oversized pupil masks have been designed to avoid pupil vignetting for up to 3% ELT pupil drifts. In case ELT pupil drifts turn out to be larger than anticipated, we could resort to more advanced post-processing techniques to (partly) mitigate this effect. For instance, we have tested ADI post-processing algorithms based on principal component analysis[11,12], and checked that there is significant room for improvement on the post-processed contrast at short angular separations.

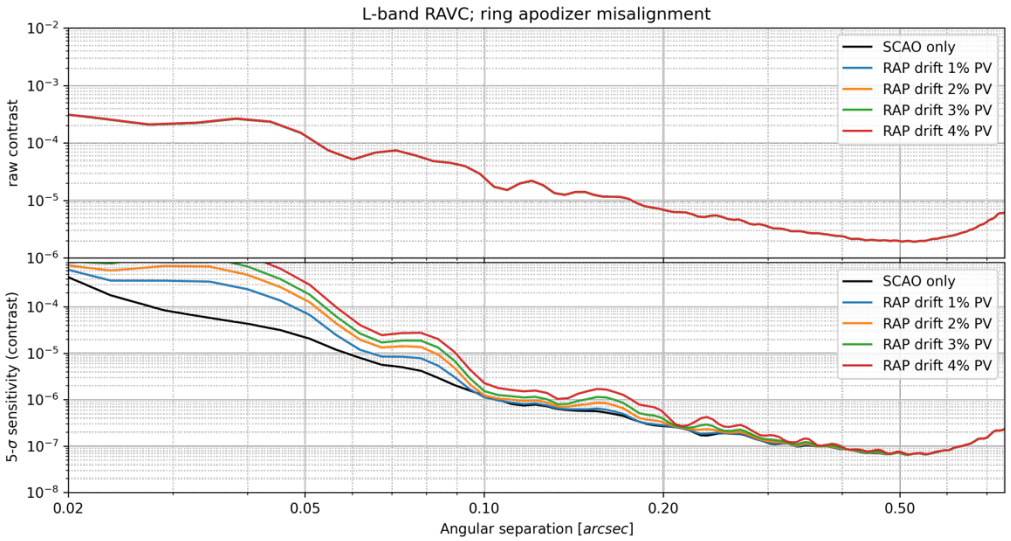


Figure 10: HCI performance in presence of various PV amplitudes of low-frequency drift in the alignment of the ring apodizer compared to the ELT pupil (top: raw contrast, bottom: ADI contrast curve).

### 4.4 Vortex chromatic leakage (RAVC and CVC modes only)

Here, we take into account the intrinsic performance of the VPMs used to implement our vortex coronagraphs in METIS. The chromatic leakage induced by VPMs is an on-axis replica of the ELT PSF, with a largely reduced intensity (typically below $10^{-2}$), which is due to the imperfect half-wave plate character of the grating used to produce the vortex phase ramp. This is a purely static contribution, which is almost perfectly cancelled by ADI processing as long as it does not create too much additional light on the science detector. In Figures 11 and 12, we show the effect of various levels of chromatic

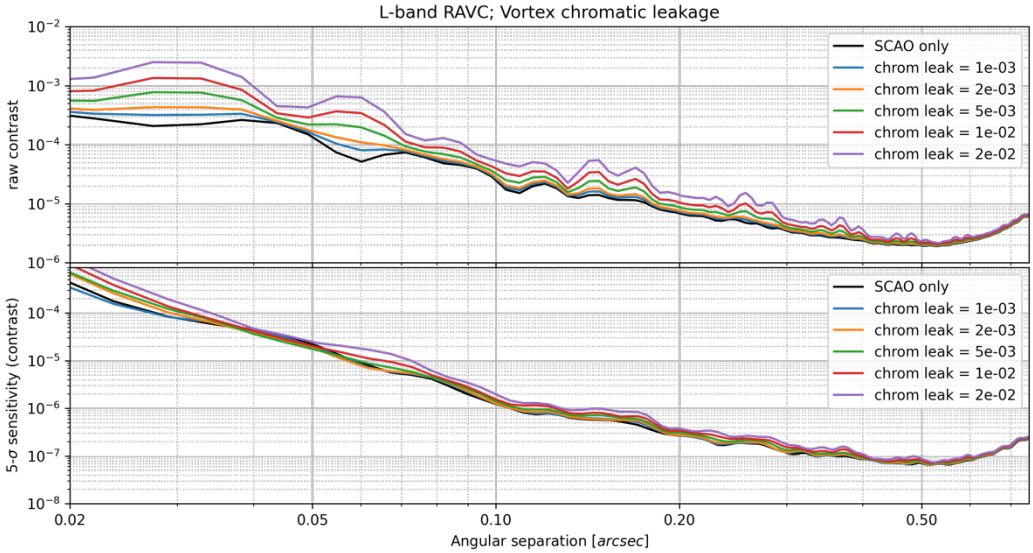


Figure 11: ADI contrast curves for the RAVC at L band in presence of chromatic leakage of various levels (averaged over the chosen filter).

leakage on HCI performance. These simulations were used to specify the acceptable level of chromatic leakage in the METIS VPMs, which are required to be smaller than $2\times10^{-3}$ at LM bands, and smaller than $10^{-2}$ at N band, computed on average over the operating wave band. With these specifications, the influence of chromatic leakage is completely negligible on post-ADI performance, and barely significant in raw contrast performance.

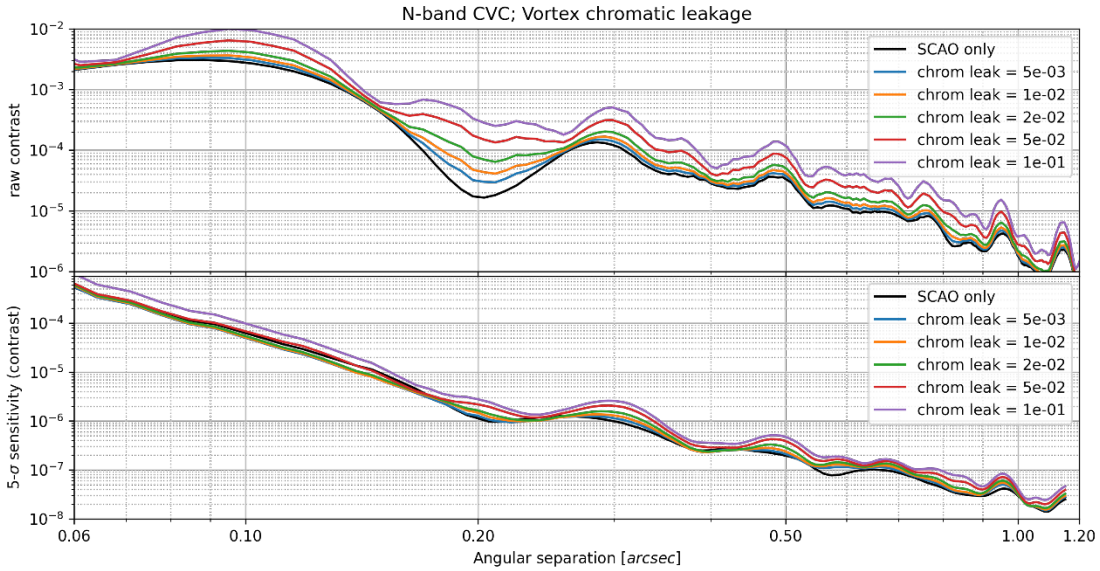


Figure 12: Same as Figure 11 for the CVC at N band.

### 4.5 Influence of residual NCPA

We explore the effect on HCI performance of residual NCPA inside the scientific camera (IMG), known to be a major contributor to the HCI performance budget, and supposed to be the limiting factor to the performance of many state-of-the-art instruments. The influence of NCPA can be divided into two main contributions: pointing errors, and higher order errors. Our simulation strategy is to feed our end-to-end HCI simulations with the output of closed-loop simulations of NCPA control with our focal-plane WFS algorithms: QACITS[13,14] for pointing errors, and PSI[15] for higher order errors. These closed-loop simulations use as input a series of NCPA sources, including static aberrations inside the instrument, chromatic beam wander due to differential atmospheric refraction between the SCAO wavelength and the IMG wavelength, and chromatic NCPA due to water vapor seeing (see Absil et al.[16] in these proceedings for more details). The latter two sources are introduced through representative time series of NCPA phase screens. COMPASS residual phase screens are also included as input to these NCPA closed-loop simulations, because residual wavefront errors appearing at low temporal and spatial frequencies in SCAO sequences would also be sensed and corrected by focal-plane WFS. Our closed-loop simulations, performed in the time domain with a pure integrator controller, also include a representative noise level for both the QACITS and PSI focal-plane WFS, based on our nominal stellar magnitude $L = 6$. The QACITS and PSI loops are both running at 1 Hz in these simulations. We additionally make the optimistic assumption that the PSI correction converges within 1 sec, while in practice PSI may take up to 10 sec to fully converge in presence of large NCPA excursions. In closed-loop operations, with relatively small NCPA perturbations on a timescale of 1 sec, this assumption should be sufficiently realistic. A full dynamical analysis of the PSI response in open loop and closed loop will be performed during METIS Phase D.

Our closed-loop NCPA control simulations are performed on a total duration of 1 hour, and the residuals of the closed-loop control are then used as input to our end-to-end HCI simulations with HEEPS. The results of these simulations are shown in Figures 13 and 14, respectively at L band and N band. Here, it is important to perform simulations at N band,

because of the highly chromatic behavior of water vapor seeing, which affects performance at N band much more than at L band. In both cases, we show separately in the figures the effects of chromatic beam wander (which also includes static NCPA) and of water vapor seeing.

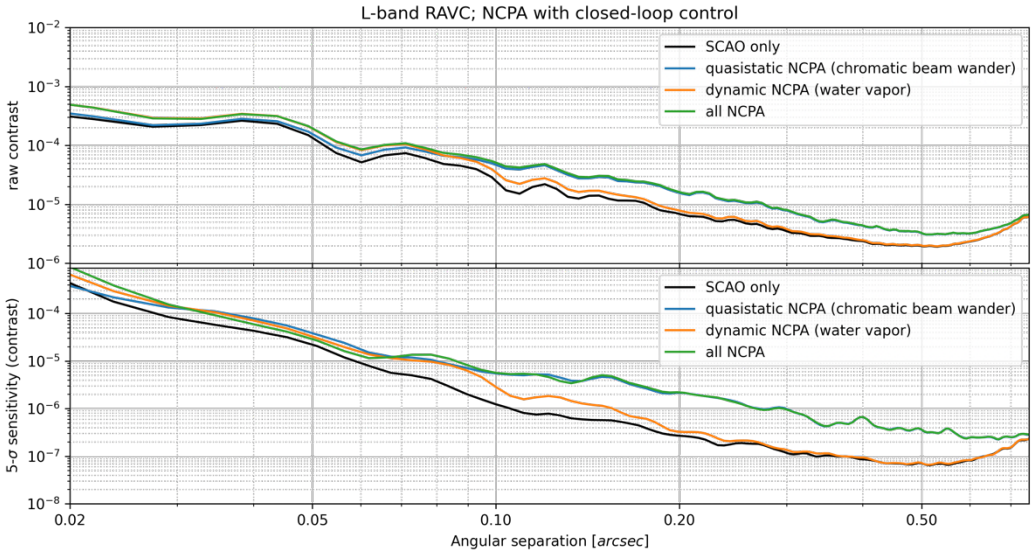


Figure 13: ADI contrast curves for the RAVC at L band in presence of all NCPA sources, taking into account closed-loop control by the METIS focal-plane WFS algorithms.

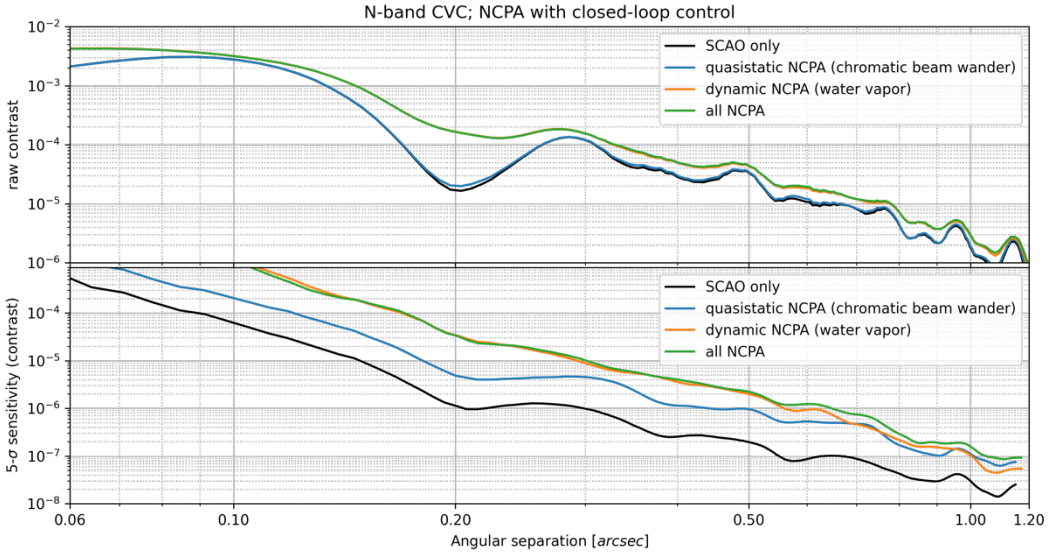


Figure 14: Same as Figure 13 for the CVC at N band.

At L band, the dominating source of NCPA is chromatic beam wander. The HCI performance after closed-loop control is somewhat above our self-defined requirement of $3\times10^{-6}$. However, we recognize that NCPA was anticipated to be the worst offender in terms of HCI performance, so this does not come as a surprise, and we are willing to allocate more error budget to this specific contributor. A possible way to improve the performance at $5\lambda/D$ (i.e., 0.″1), where the requirement

is defined, would be to extend the PSI correction beyond the 100 Zernike modes used by default, which corresponds roughly to a 5$\lambda/D$ control radius. This will be further explored during Phase D.

At N band, the situation is more problematic, as water vapor seeing degrades the post-processed contrast by about one order of magnitude, even after NCPA closed-loop control. This is all the more concerning that our simulations are optimistic about PSI's capability of providing a measurement at 1 Hz. Operating PSI at such a speed at N band cannot be taken for granted at this point, although it should be mentioned that performing focal-plane WFS at 1 Hz at N band is theoretically possible up to magnitude $N \simeq 1.5$ with a sensor noise of 50 nm or below.

### 4.6 Influence of amplitude aberrations (Talbot effect)

In addition to creating phase errors in the wavefront, aberrations inside the instrument can also lead to amplitude aberrations, due to phase aberrations being converted into amplitude aberrations upon Fresnel propagation on a distance equal to the Talbot length. A thorough description of how amplitude aberrations are simulated inside METIS is given in Boné et al. 2020[17]. In addition to the pure static aberrations described in there, we include here the effect of chromatic beam wander. This effect is related to the variable position of the footprint of the IMG beam on the METIS optics. This arises when SCAO freezes the position of the K-band beam, while differential refraction between K and LMN bands varies along the trajectory of the target across the sky. This leads to time-variable amplitude aberrations in the IMG. One of the key features of amplitude aberrations is that they have a larger influence at larger angular separations, because the Talbot length scales with the spatial frequency of the considered aberration (leading to more amplitude aberrations at higher spatial frequencies).

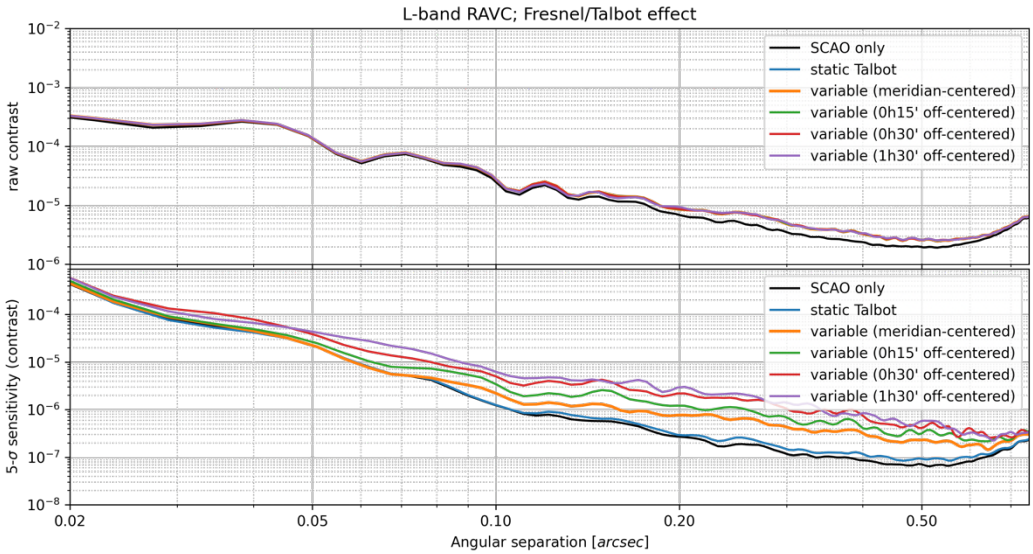


Figure 15: ADI contrast curves for the RAVC at L band in presence of time-variable Talbot amplitude aberrations due to chromatic beam wander. The center of the 1-h ADI sequence is shifted by various amounts of time compared to meridian crossing to explore the dependence of chromatic beam wander on the target trajectory in the sky.

The results of our end-to-end simulations taking into account variable amplitude aberrations due to chromatic beam wander are illustrated in Figure 15 for our 1h ADI observing sequence at L band with the RAVC. This figure also includes the effect of purely static amplitude aberrations, which are mostly negligible in the HCI performance budget. Variable amplitude aberrations, on the other hand, have a significant influence on HCI performance, although the results are still compliant with our self-defined requirement of $3\times10^{-6}$ post-ADI contrast at 5$\lambda/D$, as long as the ADI sequence is well centered around meridian crossing. For observing sequences performed further away from meridian crossing, amplitude

aberrations start to take a more significant toll on HCI performance. The underlying reason is related to the larger excursion of the LMN band beam footprint when operating farther from meridian, as the target elevation varies more over a given time span. This effect combines with a larger amount of pupil rotation on the optics upstream of the derotator, as pupil orientation directly relates to target elevation. Observing close to meridian crossing for our ADI sequences will therefore be key to maximize performance, as we have no way to compensate for amplitude aberrations within METIS. The only lever that we can act upon is to overspecify the quality of the optics located close to focal planes, which have the largest contribution to amplitude errors[17].

For the sake of completeness, we also show N-band simulations in Figure 16. The results at N band also show a large performance degradation, although the degradation is smaller than for variable NCPA after 1-Hz closed-loop control (Figure 14) up to 0.″3 in all cases, and even at larger separations when observations are performed close to meridian. The Talbot effect may have a dominating contribution at large separation for long ADI sequences, and may therefore ultimately set the detection limits for rocky planets around α Centauri.

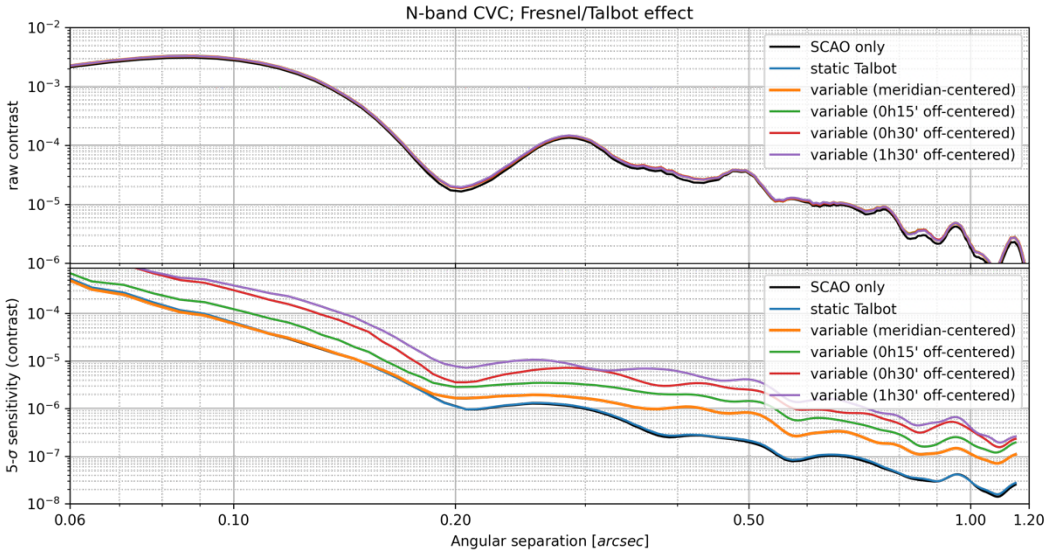


Figure 16: Same as Figure 15 for the CVC at N band.

## 5. COMBINATION OF ALL EFFECTS

In this paper, we have analyzed the effect of various instrumental and environmental parameters on the post-ADI performance of the METIS HCI modes, and defined specifications on the level of these noise sources in order to meet our contrast requirements. To conclude this study, we show how the contrast will be impacted by a combination of all these effects. For these simulations, we assume median seeing conditions and use all the default parameters for SCAO simulations, including wind-driven pointing jitter (due to wind load on the telescope structure). On the instrumental side, we include a pupil with seven misaligned segments and 10% PV segment non-uniformity (although their individual contributions are not shown for the sake of clarity), a 2% RAP pupil drift over one hour, the closed-loop residuals from the QACITS and PSI algorithms in presence of chromatic beam wander and water vapor seeing, and the variable Talbot effect due to chromatic beam wander. Chromatic leakage from the VPM is also included in the final performance, although its individual contribution is not displayed for the sake of clarity. In Figure 17, we show a representative long-exposure PSF for the RAVC at L band in presence of all these effects, to give an impression of how the raw performance will be impacted compared to the SCAO-only PSF, and of the spatial structure of the PSF.

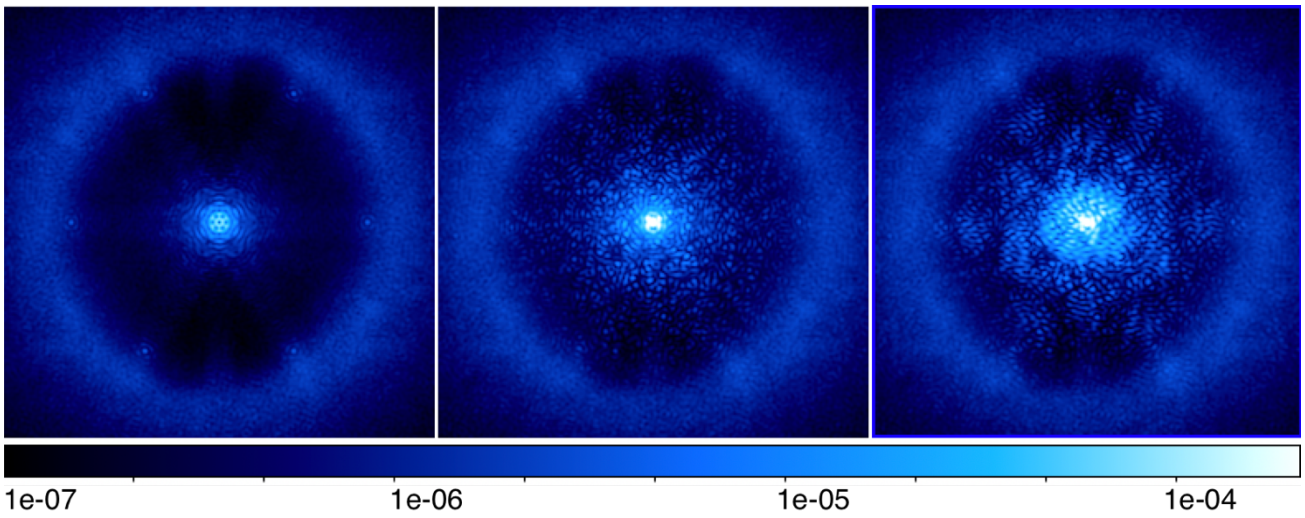


Figure 17: PSF of the RAVC resulting from a combination of errors. *Left:* SCAO only. *Middle*: "all effects" PSF of the RAVC with, in addition to SCAO residuals, 10% PV segment reflectivity, 2% PV pupil drift, 0.2% vortex chromatic leakage, Talbot effect from meridian-centered sequence, and NCPA residuals after closed-loop control. *Right*: "all effects" plus seven misaligned segments.

The final performance in presence of all noise sources is displayed in Figures 18 and 19, respectively for L band and N band. In order to keep these figures readable, we did not include the effect of thermal background, which will be discussed in the next paragraph. For the same reason, we did not include contrast curves for all individual contributors, and focused only on the most prominent ones. All contributors are still included in the "all-effects" curves.

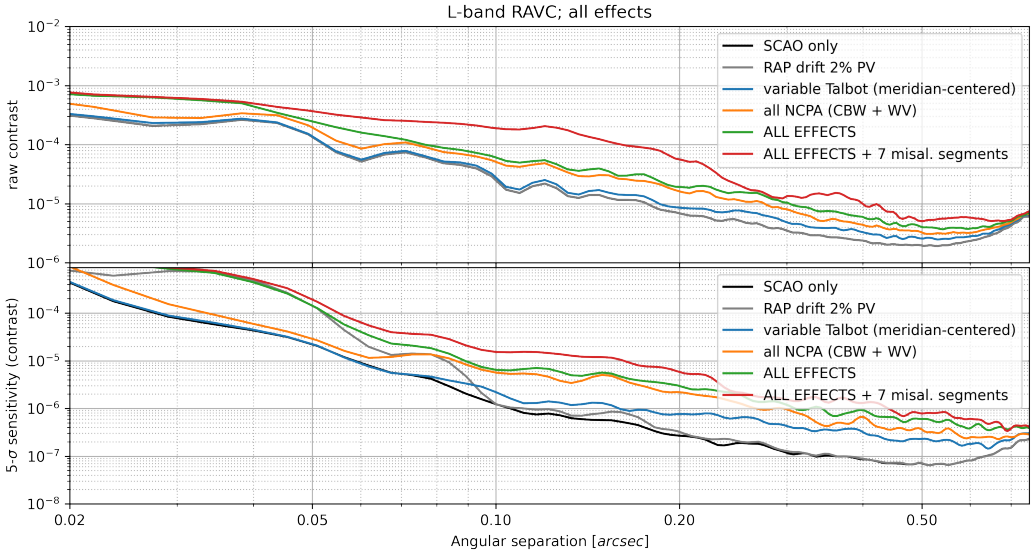


Figure 18: Summary of the HCI performance for various instrumental effects, and combination thereof (top: raw contrast, bottom: ADI contrast curve). Individual contrast curves are shown for the dominant error sources: 2% PV pupil drift, NCPA residuals after closed-loop control, and Talbot effect from meridian-centered sequence. The "all-effects" curves also include the effect of 10% PV segment reflectivity and 0.2% VPM chromatic leakage, and we also show how seven misaligned segments would further degrade the "all-effects" contrast curve.

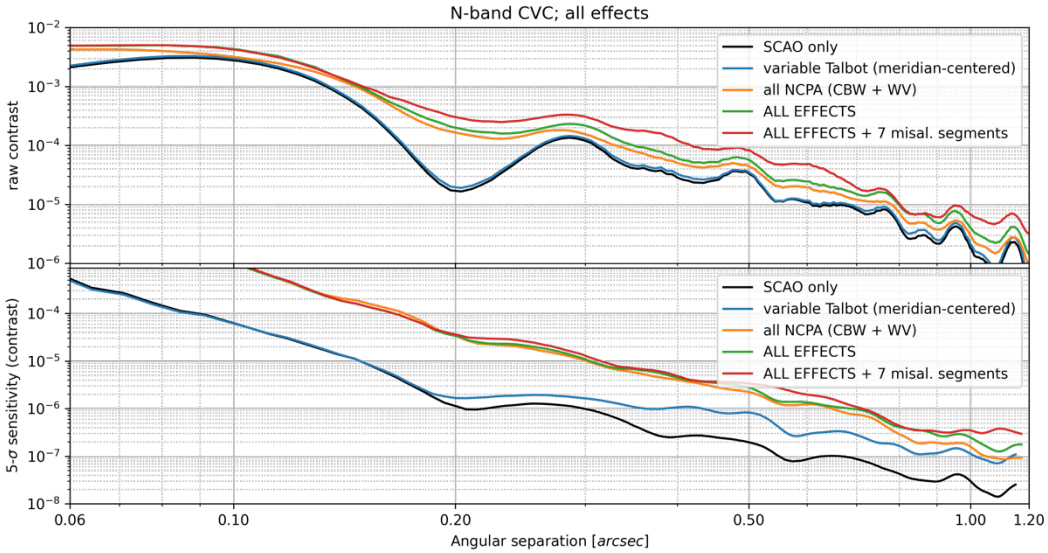


Figure 19: Same as Figure 18 for the CVC at N band and with 1% VPM chromatic leakage. Pupil drifts are not considered here, as there is no apodizer in CFO-PP1 in the case of the CVC.

The L-band performance shown in Figure 18 shows that the RAVC will be compliant with the top-level requirement of $3\times10^{-5}$ at $5\lambda/D$ (i.e., 0.″1), with a significant margin when operating on a complete ELT-M1 pupil without any misaligned segment. Even in the presence of misaligned segments, the top-level requirement can still be reached, even though performing HCI observing under such conditions should better be avoided, because it largely increases the level of starlight on the detector at the most interesting angular separations (3–10 $\lambda/D$). This figure confirms that NCPA (including non-common path pointing errors) will be the dominant error source in our HCI performance budget, which highlights the importance of optimizing the performance of the QACITS and PSI control loops during Phase D. It is also interesting to notice that RAP drifts due to pupil instabilities in the ELT is expected to drive the RAVC performance at very short separations ($< 4\lambda/D$). It should however be reminded that the situation presented here is a worst-case scenario, where a linear drift happens on the exact same timescale as the ADI observing sequence. The final performance of the ELT in terms of pupil stability will nevertheless be key for the RAVC to provide the highest performance at very short separations, as it is expected to do.

The performance at N band displayed in Figure 19 shows that NCPA variability, and water vapor seeing in particular, is driving the post-ADI performance of METIS. Yet, it should also be noticed that the Talbot effect becomes also critical for HCI performance at separations around 1.″0, especially if ADI sequences longer than 1-h (not shown here) are considered. This situation will be closely monitored during Phase D as optical components are manufactured, and in particular optical components located close to focal planes in the common fore-optics of METIS.

Finally, we show in Figures 20 and 21 a comparison of the performance of the various HCI modes included in METIS, including also the effect of thermal background noise. We also include the CLC in these figures for the sake of completeness. These figures show that the background limit will be reached in one hour for angular separations ranging from 0.″2 to 0.″3 at L band for an $L = 6$ star, while at N band in the case of α Cen, the background limit may not be reached at 1.″0 as we would have hoped in order to make the deepest possible search for temperate rocky planets. For fainter targets, the performance will generally be limited by background much closer in. These figures also highlight that the APP should be providing the deepest contrast in the range of about 6 to 18 $\lambda/D$, but that reaching the speckle-noise limit will be more difficult due to the lower throughput of that mode.

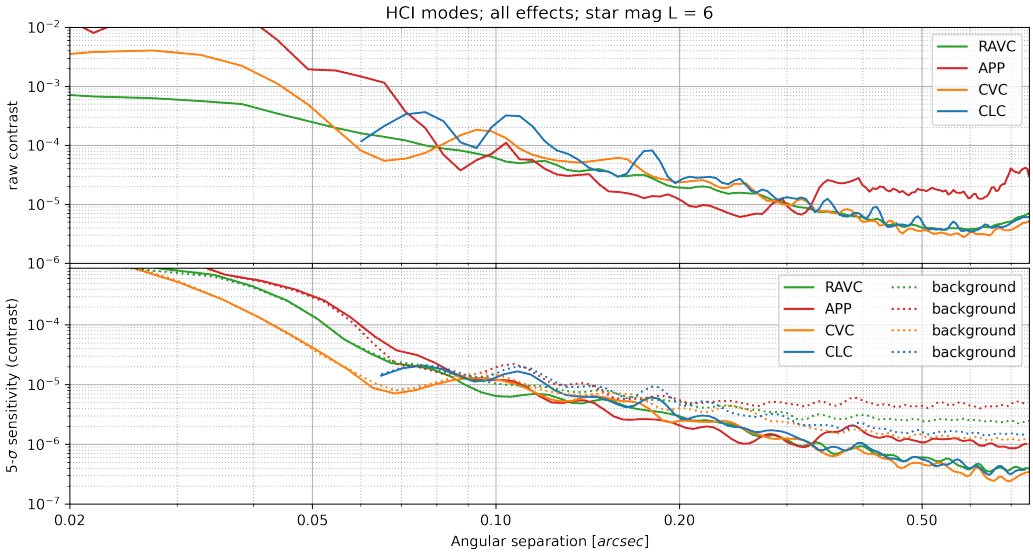


Figure 20: Summary of the HCI performance for the various METIS HCI modes at L band, taking into account all instrumental noise sources (solid curves), as well as the additional effect of thermal background noise for a star of magnitude $L = 6$ (dashed curves). The CLC is included here for the sake of completeness, as it is not part of the METIS baseline any more.

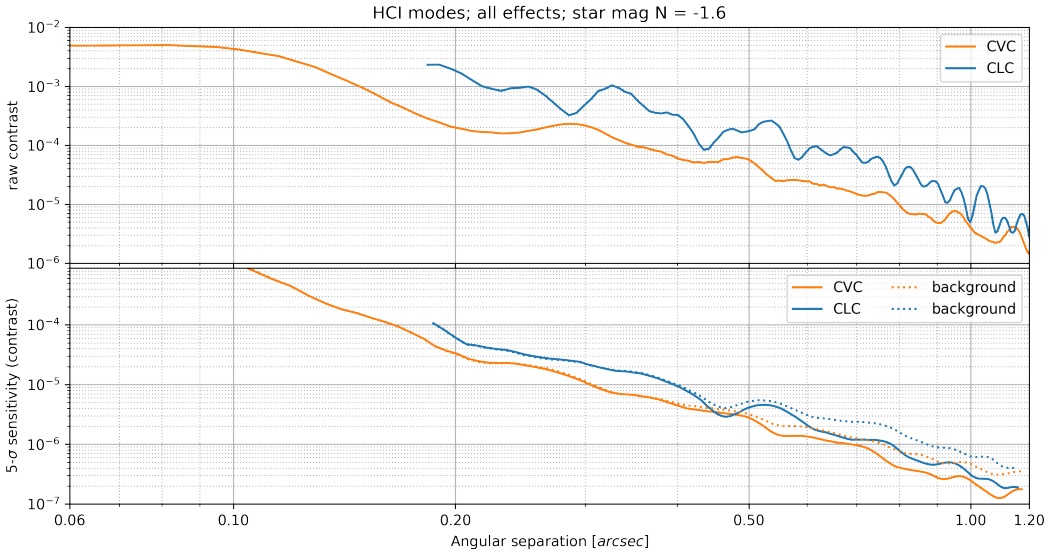


Figure 21: Same as Figure 20 at N band for the case of α Cen (magnitude $N = -1.6$).

## 6. CONCLUSIONS AND FUTURE WORK

While the analysis of HCI performance presented here is pretty comprehensive, there are still some limitations to the accuracy of our simulations. One of the main uncertainties at this point relates to the actual effect of water vapor seeing after closed-loop NCPA control at N band. The uncertainty pertains both to the exact level of the perturbation to be

corrected, and to the capability of our focal-plane WFS algorithm (PSI) to close the loop at 1 Hz at N band. This will be further explored during METIS Phase D. In particular, we are planning to explore how PSI could use the history of NCPA corrections to improve the residuals after closed-loop control, using predictive control techniques. In parallel, additional work will also be needed on the SCAO side to ensure the stability of the SCAO control loop under large NCPA slope offsets.

During Phase D, we are also planning to update our performance simulations based on the as-built properties of various optical elements and sub-systems. This will be particularly useful to better evaluate the level of amplitude aberrations due to the Talbot effect inside the instrument. We are also planning to use the output of system-level vibration analysis to feed our NCPA error budget.

## ACKNOWLEDGEMENTS

This project has received funding from the European Research Council (ERC) under the European Union's Horizon 2020 research and innovation programme (grant agreement No 819155), and from the Wallonia-Brussels Federation (grant for Concerted Research Actions).

## REFERENCES

[1] Brandl, B., Bettonvil, F., van Boekel, R., et al., "METIS: The Mid-infrared ELT Imager and Spectrograph," *The Messenger* **182**, 22–26 (2021).
[2] Mawet, D., Riaud, P., Absil, O. and Surdej, J., "Annular groove phase mask coronagraph," *ApJ* **633**(2), 1191 (2005).
[3] Delacroix, C., Absil, O., Mawet, D., Hanot, C., Karlsson, M., Forsberg, P., Pantin, E., Surdej, J. and Habraken, S., "A diamond AGPM coronagraph for VISIR," *Proc. SPIE* **8446**, 84468K (2012).
[4] Doelman, D., Snik, F., Por, E., et al., "Vector-apodizing phase plate coronagraph: design, current performance, and future development," *Appl. Opt.* **60**, D52-D72 (2021).
[5] Carlomagno, B., Delacroix, C., Absil, O., et al., "METIS high-contrast imaging: design and expected performance," *JATIS* **6**(3), 035005 (2020).
[6] Gratadour, D., Puech, M., Vérinaud, C., et al., "COMPASS: an efficient, scalable and versatile numerical platform for the development of ELT AO systems," *Proc. SPIE* **9148**, 91486O (2014).
[7] Krist, J., "PROPER: an optical propagation library for IDL," *Proc. SPIE* **6675**, 66750P (2007).
[8] Marois, C., Lafreniere, D., Doyon, R., Macintosh, B., and Nadeau, D., "Angular differential imaging: a powerful high-contrast imaging technique," *ApJ* **641**, 556–564 (2006).
[9] Gonzalez, C., et al., "VIP: vortex image processing package for high-contrast direct imaging," *AJ* **154**(1), 7 (2017).
[10] Mawet, D., Milli, J., Wahhaj, Z., et al., "Fundamental limitation of high-contrast imaging at small angles set by small sample statistics," *ApJ* **792**, 97 (2014).
[11] Soummer, R., Pueyo, L., and Larkin, J., "Detection and Characterization of Exoplanets and Disks Using Projections on Karhunen-Loève Eigenimages," *ApJ* **755**, L28 (2012).
[12] Amara, A. and Quanz, S., "PYNPOINT: an image processing package for finding exoplanets," *MNRAS* **427** (2012).
[13] Huby, E., Baudoz, P., Mawet, D., and Absil, O., "Post-coronagraphic tip-tilt sensing for vortex phase masks: The QACITS technique," *A&A* **584**, A74 (2015).
[14] Huby, E., Bottom, M., Femenia, B., et al., "On-sky performance of the QACITS pointing control technique with the Keck/NIRC2 vortex coronagraph," *A&A* **600**, A46 (2017).
[15] Codona, J. and Kenworthy, M., "Focal plane wavefront sensing using residual adaptive optics speckles," *ApJ* **767** (2013).
[16] Absil, O., Delacroix, C., Orban de Xivry, G., et al., "Impact of water vapor seeing on mid-infrared high-contrast imaging at ELT scale," *in these SPIE Proceedings* (2022).
[17] Boné, A., Tibor, A., Absil, O., et al., "The Talbot effect's impact on the high contrast imaging modes of METIS," *Proc. SPIE* **11451**, 114514D (2020).